JGR Space Physics

RESEARCH ARTICLE
10.1029/2024JA033303

Special Collection:
Space Weather Events of 2024 May 9-15

Are Supersubstorms Substorms? Extreme Nightside Auroral Electrojet Activities During the May 2024 Geomagnetic Storm

Ying Zou[1], Ohtani Shin[1], Jesper W. Gjerloev[1], Brian J. Anderson[1], Colin L. Waters[2], Chih-Ping Wang[3], Jun Liang[4], Larry L. Lyons[3], and Asti Bhatt[5]

[1]Johns Hopkins University Applied Physics Laboratory, Laurel, MD, USA, [2]University of Newcastle, Callaghan, NSW, Australia, [3]Department of Atmospheric and Oceanic Sciences, University of California, Los Angeles, CA, USA, [4]University of Calgary, Calgary, AB, Canada, [5]SRI International, Menlo Park, CA, USA

Key Points:

- We study two extreme nightside auroral electrojet events, the so-called supersubstorms, during the May 2024 storm
- The results show that only the first event is a substorm. The second event is enhancement of general magnetospheric convection
- The first and second events were driven by an internal instability in the magnetotail and external solar driving, respectively

Supporting Information:

Supporting Information may be found in the online version of this article.

Correspondence to:

Y. Zou,
ying.zou@jhuapl.edu

Citation:

Zou, Y., Shin, O., Gjerloev, J. W., Anderson, B. J., Waters, C. L., Wang, C.-P., et al. (2025). Are supersubstorms substorms? extreme nightside auroral electrojet activities during the May 2024 geomagnetic storm. *Journal of Geophysical Research: Space Physics*, *130*, e2024JA033303. https://doi.org/10.1029/2024JA033303

Received 12 SEP 2024
Accepted 15 FEB 2025

Abstract Enhancement of currents in Earth's ionosphere adversely impacts systems and technologies, and one example of extreme enhancement is supersubstorms. Despite the name, whether a supersubstorm is a substorm remains an open question, because studies suggest that unlike substorms, supersubstorms sometimes affect all local times including the dayside. The spectacular May 2024 storm contains signatures of two supersubstorms that occurred successively in time with similar magnitude and duration, and we explore the nature of them by examining the morphology of the auroral electrojet, the corresponding disturbances in the magnetosphere, and the solar wind driving conditions. The results show that the two events exhibit distinctly different features. The first event was characterized by a locally intensified electrojet followed by a rapid expansion in latitude and local time. Auroral observations showed poleward expansion of auroras (or aurorae), and geosynchronous observations showed thickening of the plasma sheet, magnetic field dipolarization, and energetic particle injections. The second event was characterized by an instantaneous intensification of the electrojet over broad latitude and local time. Auroras did not expand but brightened simultaneously across the sky. Radar and LEO observations showed enhancement of the ionospheric electric field. Therefore, the first event is a substorm, whereas the second event is enhancement of general magnetospheric convection driven by a solar wind pressure increase. These results illustrate that the so-called supersubstorms have more than one type of driver, and that internal instability in the magnetotail and external driving of the solar wind are equally important in driving extreme auroral electrojet activity.

1. Introduction

Auroral electrojets are horizontal electric currents that flow in the ionosphere of the auroral zone, and the enhanced magnitude and variability of the electrojets are known to adversely affect critical infrastructure. For instance, rapid variations of the electrojets can excite geomagnetically induced currents (GICs) by perturbing the geomagnetic field (e.g., Vorobev et al., 2019). GICs may damage high-voltage power transformers of power grids and increase steel corrosion of pipeline networks. Electrojets can heat the upper atmosphere through Joule heating (Ahn et al., 1983; Akasofu, 1981; Nisbet et al., 1982). As the heated atmosphere expands, the orbits of low-altitude satellites change. Auroral electrojets are often accompanied by auroral activity, and auroras (or aurorae) impact HF radio communication and GPS/GNSS satellite navigation by producing significant fluctuations in the electron density in the ionosphere.

Drivers of extreme auroral electrojet activities are not well understood. In this paper, extreme activity is defined as events with SuperMAG auroral indices (SMU or SML (Newell & Gjerloev, 2011)) exceeding 2,500 nT in absolute value. One example is supersubstorms, which are associated with a large westward auroral electrojet (SML $<-2{,}500$ nT) (Tsurutani et al., 2015). They often appear as isolated SML peaks (separated by >6 hr) rather than repetitive fluctuations of the index. Supersubstorms are rare events that only occur a few times per year on average (Hajra et al., 2016). They tend to occur during the main phase of geomagnetic storms, but they can also occur during non-storm times. Supersubstorms are often triggered by parcels of high-density solar wind plasma or pressure pulses with a southward IMF precursor (Tsurutani et al., 2015; Hajra et al., 2016). However, the chain of events that follows the solar wind trigger remains elusive. Existing evidence implies that supersubstorms can be a different process from typical substorms despite their name. Hajra and Tsurutani (2018) found that auroras at the peak of supersubstorms are most intense at dusk and dawn. Despirak et al. (2020, 2022) found that the westward

electrojet during supersubstorms extends globally in longitude, being largest in the post-midnight or dawn sector. Tsurutani and Hajra (2023) found that Joule heating is comparably strong on the day- and nightside, consistent with global energy dissipation. In comparison, substorms are mostly a nightside-sector phenomena with largest activity in the pre-midnight sector. The global-wide disturbance of supersubstorms in the ionosphere implies that the driver in the magnetosphere should also be widespread. Hajra et al. (2023) reported enhancement of energetic electron and proton fluxes and elevated electromagnetic ion cyclotron waves in the nightside inner magnetotail. However, these processes are also common during substorms. The mechanisms that drive the large intensity and global extent of supersubstorms are unknown.

Another type of extreme auroral electrojet activities was reported by Zou et al. (2024). The event was referred to as an auroral electrojet spike due to the transient nature, where the SML index plunged and recovered within 5 min. The short time scale also meant that the rate of change of the electrojet was unusually large. The event had a wide, if not global, span in longitude, the intensity being largest in the dawn sector, but it was narrow in latitude extent, being only 2°–3° wide. Upstream solar wind measurements showed a transient pressure pulse that was six times above the background levels. Simultaneous auroral observations suggest that the electrojet coincided with brightening of diffuse auroras. It is therefore postulated that the solar wind pressure pulse compresses the magnetosphere and enhances diffuse precipitation of electrons and protons from the inner magnetotail. The precipitation elevates the ionospheric conductivity and intensifies the auroral electrojet. This scenario offers an explanation for the wide longitudinal extent of the electrojet and the increasing electrojet intensity toward dawn. The former is because diffuse auroras extend azimuthally across many hours of MLT continuously, and the latter because electron diffuse auroras are most intense at post-midnight and morning hours.

Generally speaking, variations of the auroral electrojet can be attributed to the substorm current wedge (also called DP1 current) and/or the two-cell Hall current vortices (also called DP2 current). DP1, or Disturbance Polar type 1, is a single cell of ionospheric current system that is centered around midnight, and features a localized and intense westward electrojet in the midnight auroral oval (Akasofu et al., 1965). DP2 consists of two current cells roughly centered at the dawn and dusk terminators (Obayashi, 1967; Nishida, 1968), and are characterized by an eastward electrojet from the afternoon to midnight auroral oval and a westward electrojet from the midnight to morning oval. The two current systems are believed to correspond to different processes in the magnetosphere: DP1 to the substorm expansion phase, and DP2 to the general magnetospheric convection. It is therefore helpful to examine which current system, DP1 or DP2, dominates extreme auroral electrojet activity as this will distinguish between the type of disturbances in the magnetosphere (e.g., Clauer & Kamide, 1985; Kamide & Kokubun, 1996; Xu & Sun, 2000). DP1 and DP2 are used to describe two-dimensional current systems confined to the ionosphere, that is, equivalent current systems, although the actual current system is three-dimensional with field-aligned currents (FACs) connecting the ionosphere and the magnetosphere. The FACs that correspond to DP2 are related to the extended Region 1 and Region 2 FAC sheets that flow along the auroral oval boundaries, and those to DP1 are localized and flow upward (downward) on the western (easter) edge of the intense westward electrojet. The global extent of the auroral electrojet during supersubstorms and the auroral electrojet spike is consistent with DP2 current.

A series of extreme auroral electrojet activity occurred during the spectacular super geomagnetic storm on May 10–11, 2024, which is also widely referred to as the Mother's Day storm due to its proximity to Mother's Day, and as Gannon storm in memory of Jennifer Gannon who made outstanding contributions to space science. We focus on two electrojet events that spanned the nightside sector and both satisfy the definition of supersubstorms. The two events are interesting because despite their close proximity in time (separated by <1 hr) and similar magnitude and duration, they are driven by distinctly different processes, with one more consistent with a substorm disturbance, the other enhancement of general magnetospheric convection. This demonstrates that extreme electrojet activity has more than one type of driver, and that internal instability in the magnetotail and external driving of the solar wind are equally important in driving extreme disturbances at nightside high latitudes.

2. Data Set

The main data sets used to study the morphology of the auroral electrojets are SuperMAG and Active Magnetosphere and Planetary Electrodynamics Response Experiment (AMPERE-NEXT). *SuperMAG* is a worldwide collection of geomagnetic ground station data (Gjerloev, 2012). Undisturbed daily variations of the geomagnetic field have been subtracted, so that SuperMAG data represent perturbations of the geomagnetic field, which at

auroral latitudes are mainly produced by auroral electrojets, often by Hall current. The data have a 1-min temporal resolution.

The AMPERE-NEXT data consist of magnetic field measurements obtained from altitudes of ∼780 km by about 90 satellites (Anderson et al., 2020; Waters et al., 2020). The satellites are distributed in six equally spaced orbital planes, offering full local time coverage. In each plane, there are 11 satellites that are evenly spaced along the orbit track, providing full latitude coverage every 9 min. The AMPERE data reflect magnetic signals associated with FACs.

Disturbances in the magnetosphere are investigated using Geostationary Operational Environmental Satellites (GOES), Transition Region Explorer (TREx) RGB auroral cameras, Poker Flat Incoherent Scatter Radar (PFISR), and Defense Meteorological Satellite Program (DMSP). Specifically, GOES provides magnetic field and energetic particle data at geosynchronous orbit. TREx cameras detect auroral/airglow emissions at 557.7, 486.1, and 630.0 nm wavelengths in the auroral zone. The stations with clear sky conditions were located at Athabasca (geomagnetic 61.98°N, −72.24°E) and Lucky Lake (geomagnetic 58.5° N, −41.6°E). PFISR (geomagnetic 65.8°N, −93.6°E) probes electron density and temperature, and ion temperature and velocity in the ionosphere. Sensors onboard DMSP measure electron density, ion velocity, magnetic field, and energy spectra of electrons and ions that precipitate into the ionosphere. The parameter of most interest for this study is the ion velocity.

The solar wind conditions were provided by the high-resolution OMNI data set. OMNI contains 1-min-averaged, field/plasma data sets shifted to the Earth's bow shock nose. The OMNI data are further validated by the Magnetospheric Multiscale (MMS) satellites located right outside the bow shock.

3. Results

3.1. Geomagnetic and Solar Wind Condition

Figure 1 shows the geomagnetic condition represented by SuperMAG indices for May 10–11, 2024. The SMR index in Figure 1a exhibits a step-function like change during 1706–1820 UT on 10 May 2024, signifying the sudden commencement of the storm. SMR then reached a minimum value of −451 nT at 2236 UT, followed by a gradual recovery phase lasting for several days. Super storms of such strong intensity are very rare, and the last storm of similar intensity occurred more than two decades ago on 20 November 2003.

The SML index in Figure 1b showed several extreme westward electrojet events with SML <−2,500 nT, such as those at 1919 UT and 1949 UT on May 10 during the storm main phase, and those at 0900, 0948, and 1332 UT on May 11 during the recovery phase. In this paper we focus on the two consecutive events that occurred on May 11 at 0900 UT when the SML index plunged to −3,497 nT, and at 0948 UT when the SML index reached −3,432 nT. The close proximity in time and similar magnitude and duration of the two events seems to suggest that they are a recurrence of the same disturbance. However, as detailed below, they are produced by two distinctly different processes.

Figures 1c–1f provide zoom-in views of the indices, and in particular, Figures 1e and 1f show the regional SMU and SML indices. The regional indices reflect the local magnitude of auroral electrojets at various magnetic local times. They are calculated in the same manner as the global indices, except that they are calculated over a 3-hr sliding window in MLT (Newell & Gjerloev, 2015). For example, SML12 is centered at 1230 MLT and covers the range of 1100 MLT through 1400 MLT, and is defined as the largest negative north-south perturbation of the geomagnetic field. Although both events occurred on the nightside, their local time distribution is different with the second event being broader. Our analysis in Section 3.3 reveals that the second event actually spanned all MLTs, including the dayside. The apparent lack of dayside activity in Figure 1f was because the geomagnetic field on the dayside was perturbed in the east-west direction, rather than north-south. A detailed analysis of the two events is presented in the following sections.

3.2. First Extreme Auroral Electrojet Event

3.2.1. Morphology

Figure 2 shows the 2-D distribution of the SuperMAG geomagnetic field presumably perturbed by auroral electrojets. The perturbed fields are represented by the green vectors and have been rotated clockwise by 90° in the horizontal plane to represent equivalent ionospheric currents. The initial geomagnetic field is shown in

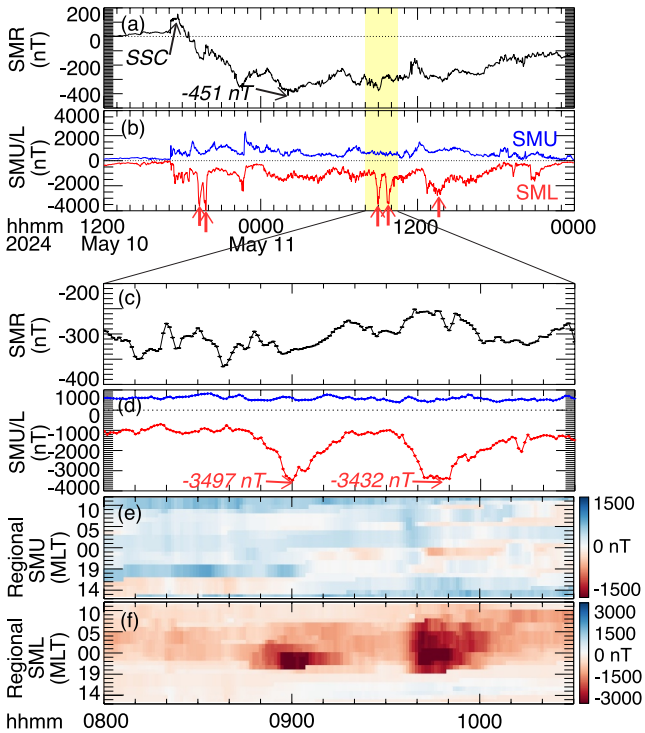

Figure 1. (a–b) Overview of the SMR, SMU, and SML indices during the May 10–11, 2024 storm. Red arrows mark SML peaks <−2,500 nT. (c–d) Zoom-in views of the SMR and SML indices during the two extreme nighttime auroral electrojet events. (e–f) Regional SMU and SML indices as a function of magnetic local time and universal time.

Figure 2a. The start of the activity is characterized by an intensification of the westward auroral electrojet over a narrow latitude band of 53°–55° MLAT and over a localized MLT range in the midnight and pre-midnight sector, as outlined by the pink contour in Figure 2b. Note that the pink contour outlines the arrows directed mostly westward, which represent the westward auroral electrojet, and arrows that are enhanced but swirl clockwise or anticlockwise poleward or equatorward of the electrojet are not included as they likely correspond to equivalent currents outside the auroral zone (Fukushima, 1971; Ohtani, 2022). The intensification quickly spread poleward, firstly to about 63° MLAT as shown in Figure 2c, and then to about 67° MLAT as shown in Figure 2d. It also spread azimuthally where the eastern edge reached about 0500 MLT in Figure 2d (beyond which there was the little change in the geomagnetic field) and the western edge reached about 2000 MLT, although the largest intensity remained at around 2100 MLT. The electrojet continued to strengthen with time and reached a peak at 0900 UT in Figure 2e. It then decayed in Figure 2f. The decay was mostly confined to the pre-midnight and midnight sectors, and the electrojet in the post-midnight sector remained elevated.

Figure 3 shows the AMPERE magnetic field presumably perturbed by FACs. Figures 3a–3d show the 2-D distribution of the perturbed field represented by the color vectors. Different colors represent measurements from the different satellites in the Iridium constellation. Figure 3a shows the magnetic field before the event onset. Following the onset, AMPERE recorded remarkably large westward perturbations at 52°–57° MLAT and 2100–2300 MLT (see the poleward portion of the pink dashed contour in Figure 3b), indicating enhancement of upward (downward) FACs on the equatorward (poleward) side of this latitude band. The perturbation also extended to 0100 MLT, although of a smaller magnitude. Changes of magnetic field at other meridians were small, suggesting that the FACs were localized in local time. A large eastward perturbation occurred equatorward of the large westward perturbation along 2100 MLT (see the equatorward portion of the pink dashed contour). This formed a latitudinal shear, implying intense upward FAC at 2100 MLT. Interestingly, the local time of this FAC coincides with the large westward electrojet seen in the SuperMAG data in Figure 2c.

As the event developed, the region of perturbation extended eastward, first to 0100 MLT in Figure 3c, then to about 0600 MLT in Figure 3d. The perturbation in the pre-midnight sector did not disappear but decreased in magnitude, and the direction of the magnetic field also returned toward the pre-onset direction. The eastward extension of FACs is consistent with the spreading of the electrojet seen in the SuperMAG data in Figure 2d, and the latitudinal location of the newly extended FACs, which were positioned at about 50°–60° MLAT, also agreed with that of the electrojet. However, SuperMAG data suggest that the electrojet remained largest in the pre-midnight sector, whereas the AMPERE FACs weakened there. We postulate that the difference was because SuperMAG captures the divergence-free component of the current system, which is, to a first approximation, a Hall current. AMPERE captures the rotation-free component, which closes in the ionosphere as Pedersen currents.

For a better presentation of how FACs varied with time, Figure 4 shows AMPERE data in the time series format. In particular, Figures 4b–4e show the geomagnetic east-west perturbation of magnetic field measured along a given orbit plane (the MLT (rounded) at which the plane intersected 60° MLAT was labeled in the vertical axis title). The measurements appear as slant stripes because they are taken by satellites that move poleward/equatorward with time, The magnetic field in Figures 4b–4e exhibit the same key features as those shown in Figure 3, with an enhancement of the westward magnetic field to >1,000 nT centered at around 55° MLAT. The enhancement first occurred at 2100 and 2300 MLT (highlighted by the green arrows in Figures 4d and 4e), then propagated to 0100 and 0400 MLT (Figures 4b and 4c). Figures 4b and 4c further show thinning and equatorward displacement of the auroral oval before the event onset, and poleward expansion of the auroral oval after the onset. For instance, as indicated by the green dashed line in Figure 4b, the area of westward magnetic field (colored in

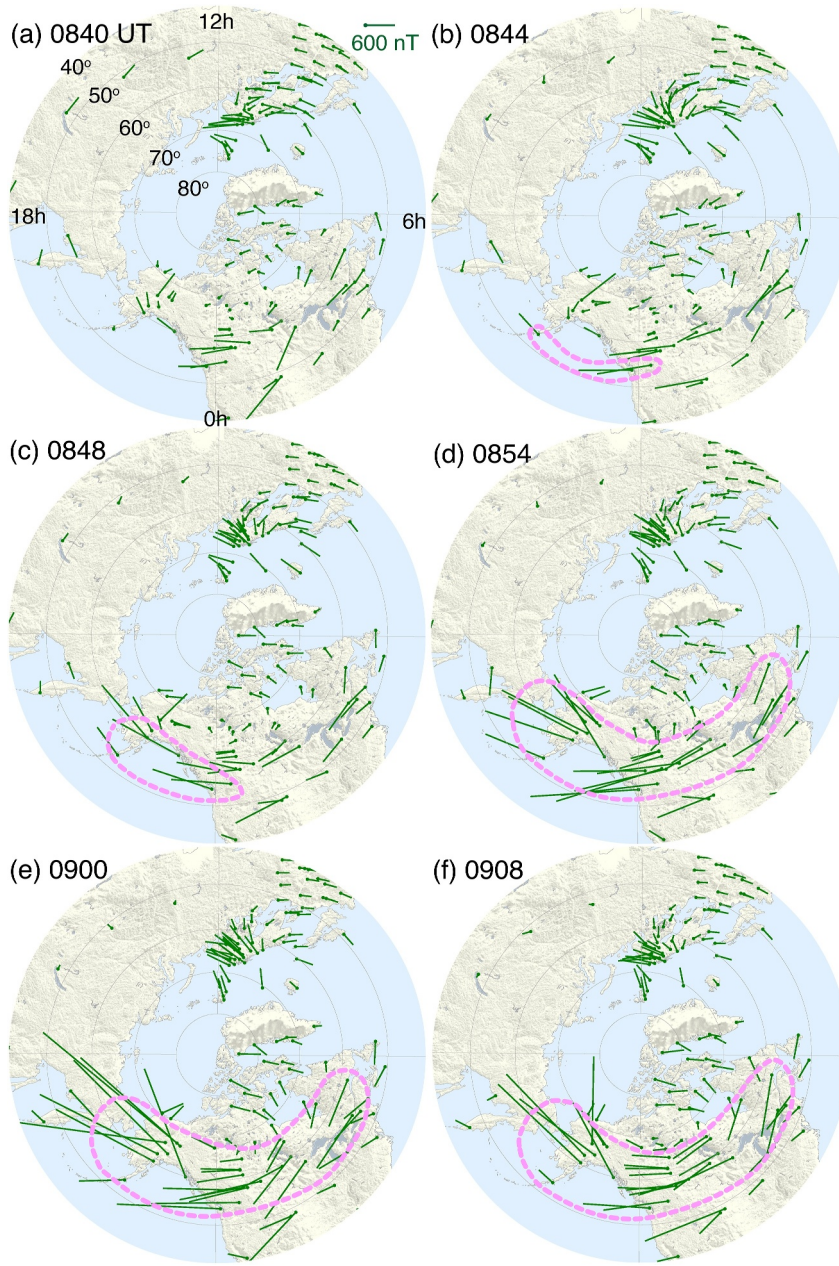

Figure 2. 2-D distribution of SuperMAG geomagnetic perturbation (represented by the green vectors) in MLAT-MLT coordinates at selected UT times on 11 May 2024. The green vectors have been rotated clockwise by 90° to represent equivalent ionospheric currents. The pink dashed contours delineate regions with enhanced perturbation.

red) at 0400 MLT narrowed and shifted equatorward up to 0840–0850 UT, and expanded poleward afterward. This evolution is representative of the behavior of the auroral oval because a latitudinal gradient of the azimuthal field indicates FACs (a positive gradient corresponds to downward FACs, which in the post-midnight sector suggests R1 FAC), and large-scale R1/2 FACs flow on the poleward and equator edge of the auroral oval.

Figure 4f shows the east-west perturbations of the magnetic field as a function of MLT. The data were averaged over 52°–57° MLAT, where the magnetic field was strongly perturbed. The measurements appeared as short colored strokes with breaks in between in the time series plot because one satellite crosses 52°–57° MLAT for <2 min, and the separation between consecutive satellites is 9 min. We smoothed the measurements by 5 min to make the data more visible. Figure 4f clearly shows the sudden enhancement of the westward magnetic field at

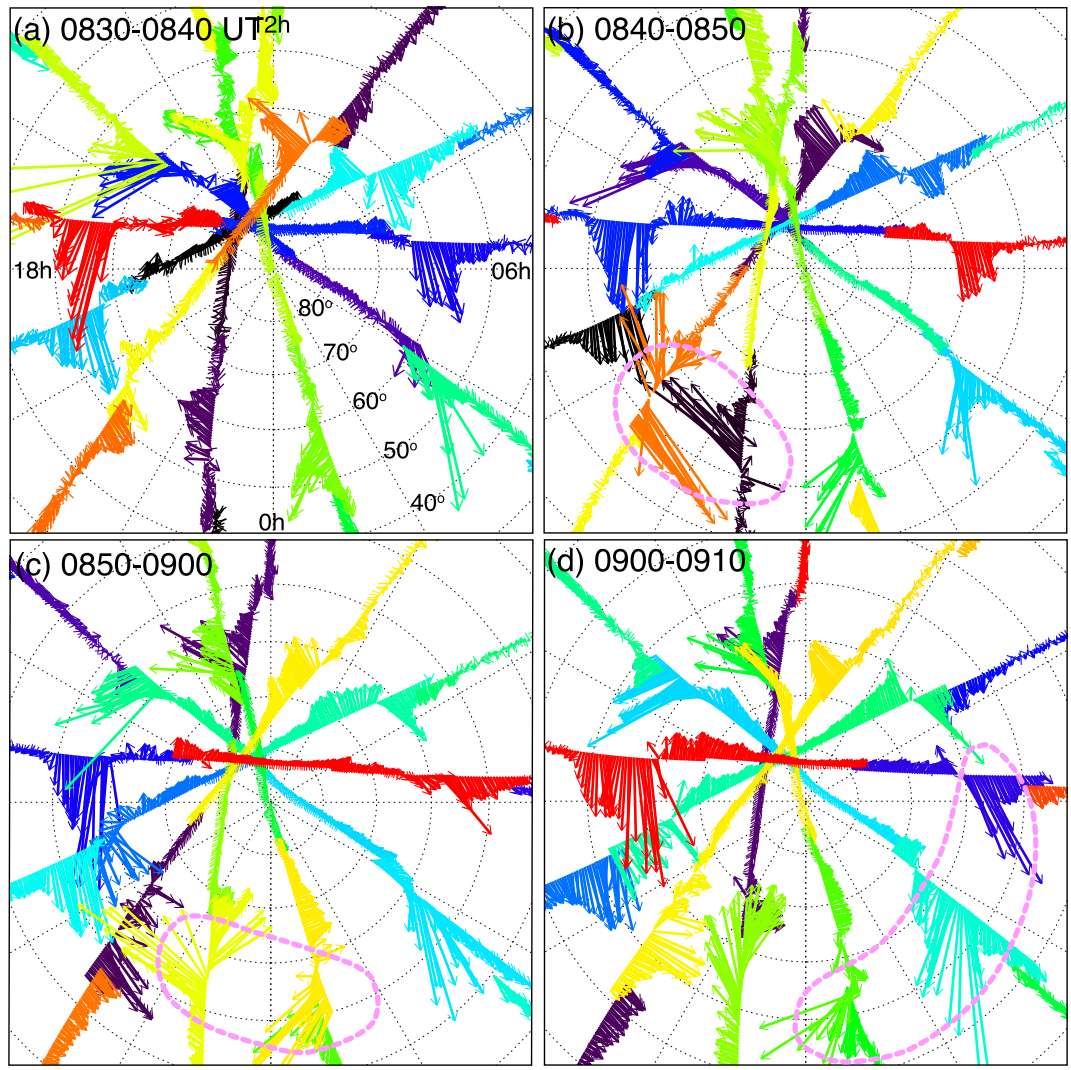

Figure 3. 2-D distribution of AMPERE magnetic perturbations in MLAT-MLT coordinates on 11 May 2024. The pink dashed contours delineate enhanced perturbation of the field.

2100–2300 MLT with propagation to 0100, 0400, and then 0600 MLT. At each MLT, the enhancement persisted for about 20 min, except at 0600 MLT where it did not decay but showed a second enhancement after 0935 UT. The second enhancement coincides with the second extreme auroral electrojet event discussed in detail in Section 3.3.

Note that a rapid increase of currents at a localized region followed by a poleward and azimuthal expansion is characteristic of a substorm expansion phase, and the substorm growth phase is associated with thinning and equatorward shift of the auroral oval. Therefore, the morphology of currents revealed by SuperMAG and AMPERE implies that the enhanced auroral electrojet resembles DP1 current, and that the first event is likely to have been associated with a substorm.

3.2.2. Magnetospheric Driver

Substorms are associated with an organized sequence of auroral display. The expansion phase can be uniquely identified as a sudden brightening along a pre-existing growth-phase arc and a subsequent poleward and azimuthal expansion (Akasofu, 1964). Figure 5 shows the auroral observations from the TREx RGB camera at Athabasca (geomagnetic 61.98°N, −72.24°E, located at around 0100 MLT). A movie of the auroral observations is provided as Movie S1 in the supplementary material. Figure 5a corresponds to the end of the growth phase, where faint azimuthally aligned auroral arcs drifted equatorward. The equatorward portion of the auroral oval was

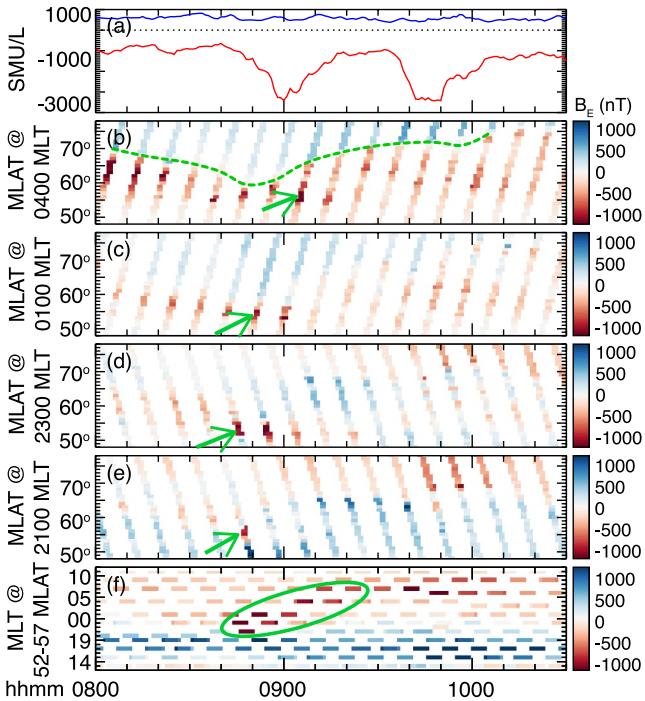

Figure 4. Time series of AMPERE magnetic perturbations on 11 May 2024. (a) SMU and SML indices, which is the same as Figure 1d. (b)–(e) Latitudinal distribution of AMPERE magnetic perturbations along selected orbital planes. The intersection of the orbital plane with 60° MLAT (rounded to the nearest hour) is labeled. The green arrows mark the enhancement of perturbation to >1,000 nT. (f) MLT distribution of AMPERE magnetic perturbations within 52°–57° MLAT. The green contour highlights the enhancement of perturbation and its propagation toward dawn.

outside the camera FOV. Starting around 0846 UT, the camera captured brightened auroras in the southwestern corner. The brightening was weak in Figure 5b, probably because the brightening originated equatorward of the camera and the camera only captured the high-altitude portion of the auroral emissions. The weak emissions were followed by bright green emissions in Figure 5c, which were followed by expansion of green emissions in both poleward and azimuthal direction in Figure 5d. The brightened auroras exhibited distinct ray structures. The expansion continued and swept across the FOV (Figures 5e and 5f), and the camera observed dynamic arcs and folds. The sequence of auroral evolution indicates a classic substorm expansion phase with an auroral bulge which initiated at the equatorward portion of the auroral oval and rapidly expanded. The TREx station at Lucky Lake (geomagnetic 58.5°N, −41.6°E) also captured the azimuthal expansion of the auroral bulge, as seen in Movie S2.

The main magnetospheric signatures of a substorm expansion phase include thickening of the plasma sheet, magnetic field dipolarization, and energetic particle injections. Figure 6 shows the magnetic field and energetic particle fluxes at geosynchronous orbit measured by GOES. GOES 18, which was positioned near midnight, initially observed a highly stretched, tail-like magnetic field. The inclination of the field (angle of the magnetic field vector deviating from the GSM Z direction) was close to 90°. The inclination began to decrease at around 0843 UT, signifying the onset of magnetic field dipolarization. The dipolarization indicates that the cross-tail current was diverted into the auroral ionosphere, establishing the substorm current wedge. The dipolarization was accompanied by an expansion of the plasma sheet, because the northward magnetic field component increased while the total field strength decreased, which suggests that the satellite, originally located at the outer plasma sheet, now found itself closer to the neutral sheet. As the satellite approached the neutral sheet, it detected sharp increases of energetic electron and proton fluxes, indicative of energetic particle injections.

GOES 16, which was positioned in the post-midnight sector, observed similar changes but with a delay. For instance, the dipolarization started at around 0852 UT, nearly 10 minutes later than GOES 18. The delay implies azimuthal expansion of the disrupted cross-tail current, which is a typical signature of substorms (Nagai, 1991; Watson & Jayachandran, 2009), and is in excellent agreement with the azimuthal spreading of the auroral electrojet observed by SuperMAG and the eastward propagation of FACs observed by AMPERE. The GOES measurements therefore support the notion that the extreme auroral electrojet was driven by a substorm disturbance in the magnetotail.

3.3. Second Extreme Auroral Electrojet Event

3.3.1. Morphology

We now describe the second extreme event and compare it with the first event. Figures 7a–7c present the 2-D distribution of the SuperMAG geomagnetic field in a similar format as Figures 2 and 7d–7l present the measurements at individual stations. The selected stations include those located at the dayside at around 1200 MLT (Panels d–e), in the post-midnight at around 0300 MLT (Panels f–h), and in the pre-midnight sector at around 2200 MLT (Panels j–l). A station located at around 0100 MLT was also selected (Panel i) because it was among the equatorward-most stations that captured the electrojet. The key feature of the event is that the auroral electrojet was intensified simultaneously over a broad local time and latitude range (Figure 7b). By simultaneous, we refer to the increase of geomagnetic field perturbation starting approximately within ±1 min from 0935 UT considering that the increase on the nightside was gradual without a clean-cut onset. The latitudinal range spanned about 54°–65° MLAT (see the simultaneous onset indicated by the pink vertical dashed line in Figures 7f–7g and 7i, as well as in Figures 7j and 7k), although the lower latitude estimate was limited by the sparse stations within 50°–60° MLAT in North America. The local time range extended from the pre-midnight sector to magnetic noon (see the

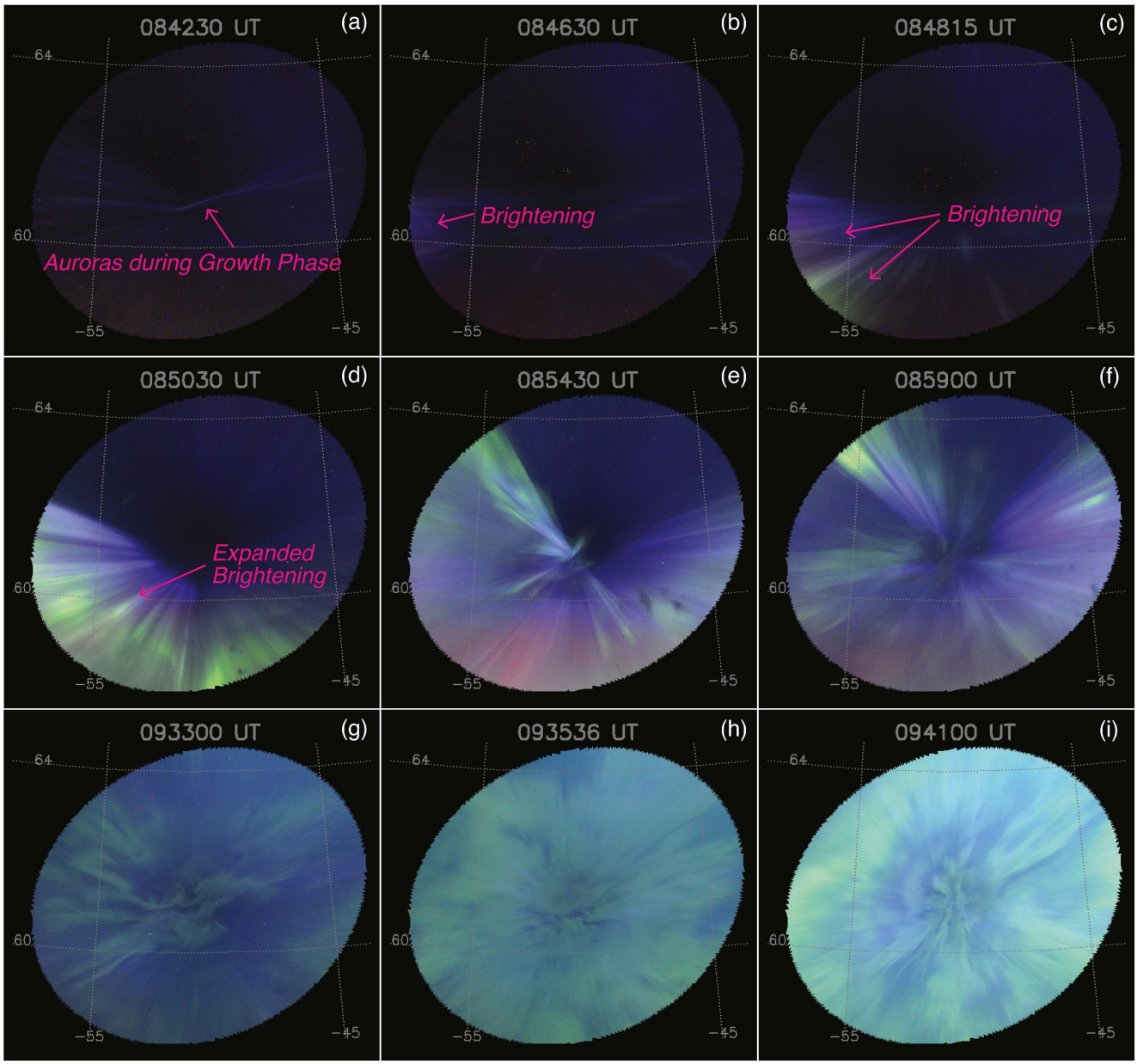

Figure 5. Snapshots of TREx RGB observations of auroras at Athabasca on 11 May 2024. The time instance when the images were taken were labeled at top. Panels (a–f) correspond to substorm expansion phase of the first event, and Panels (g–i) correspond to the enhancement of general magnetospheric convection of the second event.

simultaneous onset across Figures 7d–7e, 7f–7g, 7i, and 7j–7k), and possibly even to the afternoon hours into Russia where the stations were sparse. Such a broad onset is quite different from the first event. The intensified electrojet was directed westward in the night sector, equatorward at noon, eastward in the afternoon sector. The westward electrojet on the nightside still extended poleward, as seen from the delayed perturbation of the magnetic field at stations above 65° MLAT (Figures 7h and 7l). However, the development of the electrojet at those stations coincided with the decay of the electrojet at stations located around and below 60° MLAT (Figures 7f, 7i, and 7j). This is consistent with an overall poleward shift of the electrojet (Figure 7c).

Figures 8a–8c show the 2-D distribution of the AMPERE perturbed field before, during and after the extreme electrojet activity, respectively. The event is characterized by field enhancement across the entire polar region, most evident in the dawn and dusk sectors. As the event ended, the enhancement subsided, except for a limited region in the afternoon quadrant below about 60° MLAT. Large-amplitude localized FACs, like those that

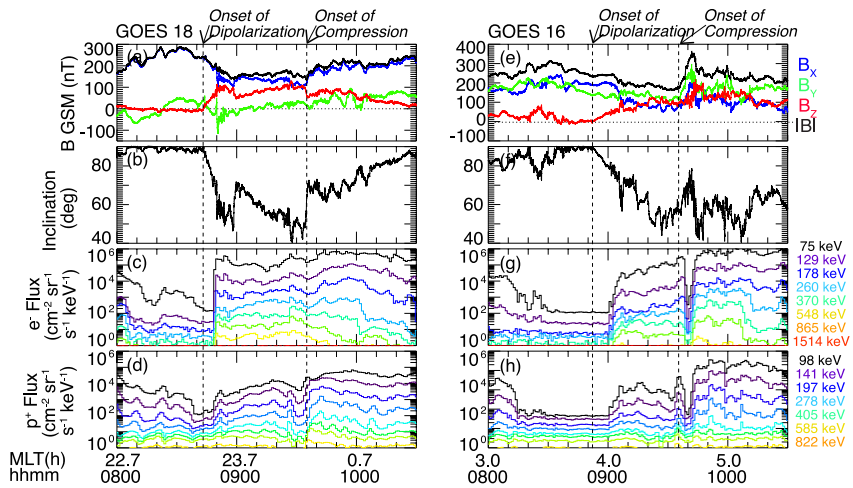

Figure 6. (a–b) Magnetic field and inclination angle. The inclination angle is defined as the angle of the magnetic field vector deviating from the GSM *Z* direction. (c–d) Energetic electron and proton fluxes as measured by GOES 18 (G18) on 11 May 2024. (e–h) Similar to Panels (a–d) but for G16.

characterized the first event, did not occur here. In fact, Figures 4b–4e suggest that the intense midnight FACs that signified the onset of the first event did not recur for the second event. Instead, as indicated in Figure 4f, the event was associated with a modest enhancement of the background magnetic field at dawn and dusk.

The enhancement shown in Figure 4f occurred at the equatorward edge of the auroral oval, and Figures 8e–8h present the time evolution of the magnetic field at the poleward portion of the auroral oval and in the polar cap. Four MLTs are shown, which are 0700 MLT (Figure 8e), 2300 MLT (Figure 8f), 1900 MLT (Figure 8g), and 1300 MLT (Figure 8h). Note that the color scale has been blue or red shifted in order to highlight the variation of the field. Several important features are evident. First and foremost, the background field above 65° MLAT was enhanced in the eastward direction at 0700 MLT, and westward at 2300, 1900, and 1300 MLT (highlighted by the green arrows). Secondly, the enhancement occurred roughly around the same time across MLTs. The slight delay at 2300 and 1900 MLT is likely because the satellites did not enter the region of interest (i.e., polar region) until a few minutes after the event onset. The extended extent of the enhancement in latitude and longitude suggests that the associated FACs were large-scale. Next, the time when the enhancement commenced, peaked, and recovered agreed with the auroral electrojet activity represented by the SML index (Figure 8c). Finally, the MLT distribution of the enhancement in the polar cap is similar to that at the equatorward edge of the auroral oval, both peaking at dawn and dusk, as seen in Figures 8i and 8k. The direction of the enhanced field is opposite between the two latitude bands, forming a shear. The sense of the shear is consistent with the Region-1 FACs which flow into (out of) the ionosphere at dawn (dusk). Therefore, the AMPERE data suggest an intimate relationship between the development of the extreme auroral electrojet and the strengthening of large-scale Region-1 FACs.

3.3.2. Magnetospheric Driver

The different morphology of the auroral electrojet and associated FACs between the first and second events suggests that they are driven by different types of disturbances in the magnetosphere. Indeed, the second event was not accompanied by signatures of substorms, such as poleward expansion of auroras and/or dipolarization of magnetic field in the magnetotail. The auroras were enhanced simultaneously across the entire sky (Figures 5g and 5h, although the enhancement was not steady but pulsated over time), and the magnetic field was stretched at midnight (Figure 6). The fact that the auroral electrojet in the second event resembles DP2 current indicates that the event was probably caused by an enhancement of magnetospheric convection.

The strength of the magnetospheric convection can be quantified as the convection electric field, and we examine the convection electric field measured by PFISR and DMSP. Figure 9 shows the PFISR measurements, which were obtained at around 2230 MLT, the longitudinal peak of the auroral electrojet. Immediately after the event onset at around 0935 UT, PFISR observed strong ionization in the E region ionosphere (95–130 km in Figure 9a),

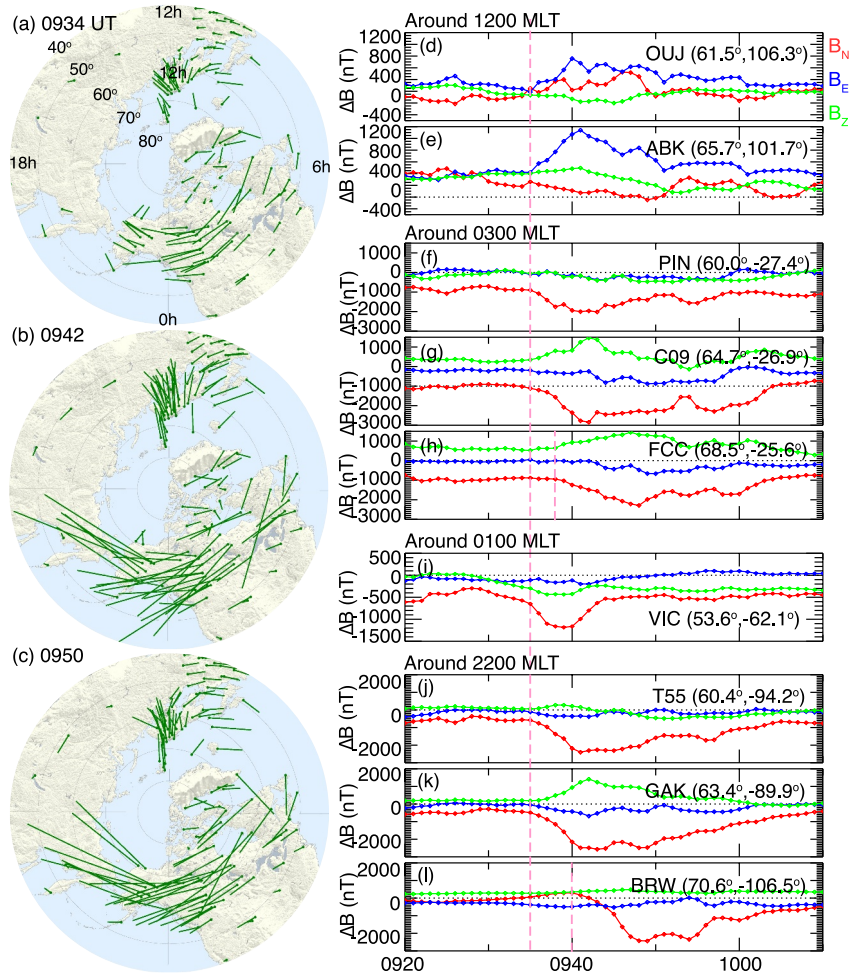

Figure 7. (a–c) 2-D distribution of SuperMAG geomagnetic perturbations in MLAT-MLT coordinates at selected instances (rotated clockwise by 90° to represent equivalent ionospheric currents) on 11 May 2024. (d–k) Geomagnetic perturbations recorded at individual stations located at around 1200 MLT (Panels d–e), 0300 MLT (Panels f–h), 0100 MLT (Panel i), and 2200 MLT (Panels j–l). The pink dashed vertical lines mark the onset of the local perturbation.

suggesting increased precipitation of energetic particles from the magnetosphere. The precipitation continued until 1000 UT before returning to the pre-event level. The eastward plasma convection changed from <400 m/s before the event onset to up to 1,000 m/s after the onset (Figure 9b). Since motion of plasma in the F region ionosphere is governed by the electric field drift, the increase of the eastward convection suggests an enhancement of the convection electric field in the northward direction, and hence the magnetospheric convection. The eastward convection decreased during 0950–1000 UT, which was also the time when the auroral electrojet activity declined, and then fluctuated around 600 m/s until the end of the interval. The northward convection did not exhibit any substantial change.

One may wonder whether the enhanced precipitation and convection electric field measured by PFISR can account for the extreme magnitude of the electrojet, and if so, the enhancement of which parameter plays a more important role. This might be estimated with a back-of-the-envelope calculation, where we predict how much the geomagnetic field would be disturbed given the PFISR-measured precipitation and electric field, and compare this with the disturbance recorded by the magnetometer. The prediction involves two steps, which are obtaining the current density of the electrojet based on PFISR-measured precipitation and electric field, and assessing the disturbance of the magnetic field. Two assumptions are used. Firstly, the auroral electrojet is dominated by Hall current. The current density of the auroral electrojet per unit length can then be obtained using Ohm's Law as

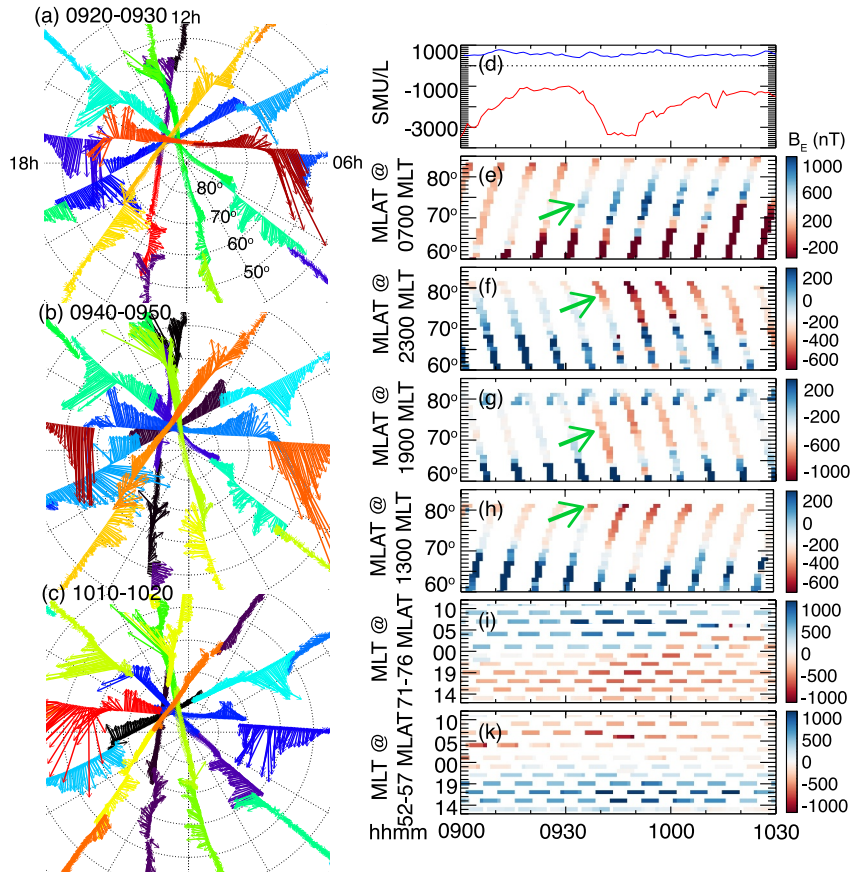

Figure 8. (a–c) 2-D distribution of AMPERE magnetic perturbations in MLAT-MLT coordinates on 11 May 2024. (d) SMU and SML indices. (e–h) Latitudinal distribution of AMPERE magnetic perturbations along selected orbital planes. The intersection of a given orbital plane with 60° MLAT (rounded to the nearest hour) is labeled in the *Y* axis title. The green arrows mark the onset of FAC change. (i–j) MLT distribution of AMPERE magnetic perturbations over given latitude bands. The latitude ranges are labeled in the *Y* axis title.

$$J = \Sigma_H E \tag{1}$$

where Σ_H represents the Hall conductance (height-integrated Hall conductivity), and E represents the electric field. The second assumption is that the auroral electrojet can be approximated as an infinite sheet of current following horizontally in the ionosphere. Disturbance of the geomagnetic field can be obtained as the field of an infinite current sheet, which according to Ampere's Law is

$$\Delta B = \frac{1}{2}\mu_o J \tag{2}$$

where B represents the geomagnetic field, μ_o represents the vacuum magnetic permeability, and J represents the density of the auroral electrojet per unit length.

The PFISR-predicted geomagnetic disturbance can hence be obtained by combining Equations 1 and 2 as

$$\Delta B = \frac{1}{2}\mu_o \Sigma_H E \tag{3}$$

The Hall conductance was determined in the same way as described by Wang and Zou (2022) based on the ionization profile in Figure 9a with additional information such as ion composition, electron-neutral and ion-neutral collision frequencies, and the local magnetic field. PFISR provides estimates of ion composition. The

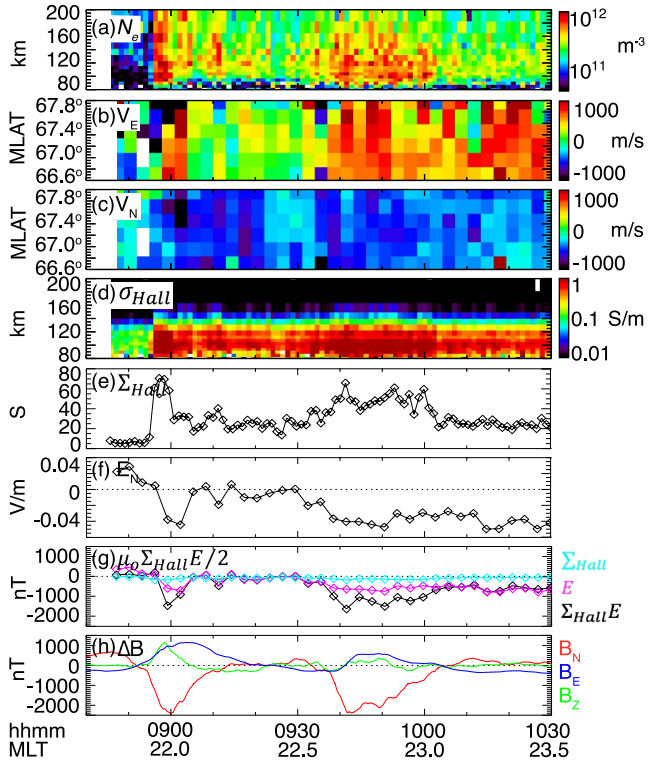

Figure 9. (a) Electron density as a function of altitude measured by PFISR on 11 May 2024. (b)–(c) East- and northward plasma convection velocity as a function of MLAT. (d) Hall conductivity as a function of altitude. (e) Altitude-integrated Hall conductivity, namely Hall conductance. (f) MLAT-averaged electric field in the northward direction. The electric field was averaged over 66.5°–67.0° MLAT. (g) Black line: magnetic perturbation predicted based on PFISR-measured Hall conductance and electric field. Magenta line: magnetic perturbation predicted based on PFISR-measured electric field, where the Hall conductance was kept the same as that prior to the event. Cyan line: magnetic perturbation predicted based on PFISR-measured precipitation, where the electric field was kept the same as that prior to the event. (h) Magnetic perturbation measured by Poker Flat ground magnetometer.

collision coefficients were taken from Schunk and Nagy (2009), the neutral densities from MSIS (Picone et al., 2002), and the local magnetic field was from the International Geomagnetic Reference Field (Thébault et al., 2015). The ionization profile in Figure 9a was taken from the radar beam that looks vertically upward, whereas the electric field in Figure 9f was inferred mainly based on beams that probe east and west. When taking the product of the two parameters in Equation 3 we have assumed spatial uniformity across beams (about 1° in MLAT and 10° in MLON). We mainly focus on the north-south component of ΔB, as the geomagnetic field is mainly disturbed in this direction and the north-south component is what is used to construct the auroral electrojet indices.

As shown in Figure 9g, PFISR predicts that the geomagnetic field exhibits two major disturbances (black curve), the first one peaking at around 0859 UT (time cadence being 3 min), and the second one peaking at around 0942 UT. The magnitude of the disturbances is significant, being about −1,471 and −1,638 nT, respectively. The predicted variation is qualitatively consistent with the local geomagnetic field perturbation measured at Poker Flat shown in Figure 9h, although the amplitude is smaller by about 29% for the disturbance at 0942 UT and 37% for the disturbance at 0859 UT. The smaller amplitude is likely because the electrojet had a latitudinal peak equatorward of Poker Flat, as implied by the downward magnetic component (green) in Figure 9h. PFISR might therefore have missed the most intense precipitation associated with the electrojet. The electrojet might also contain spatial gradient rather being an infinite current sheet. Nevertheless, the fact that PFISR predicts nearly 70% of the geomagnetic field perturbation suggests that the enhanced precipitation and convection electric field at PFISR can explain most of the large variation of the electrojet.

Both particle precipitation and electric field increased during the enhanced electrojet, but to evaluate which parameter makes the major contribution to the extreme electrojet, we predict how much the geomagnetic field is disturbed if only the precipitation increased (assuming no change in the electric field from the pre-event level, which is taken as 0910–0935 UT), and only electric field increased (no change in the precipitation). If only the electric field increased, the geomagnetic field (magenta curve in Figure 9g) would still undergo an evolution trend consistent with the SML index and the local geomagnetic field, but the amplitude would be smaller by half compared with the situation when both parameters increased. If only the precipitation increased, the geomagnetic field (cyan curve in Figure 9g) would exhibit very subtle time variation because of the near-zero electric field. We therefore conclude that the convection electric field has a major role in the development of the auroral electrojet activity.

Although we primarily use PFISR measurements to understand the driver of the second event, PFISR was also located at a favorable location for the first event. In particular, the data from PFISR show intense and transient precipitation right at the event onset, likely in association with the substorm auroral bulge. Plasma convection was also enhanced in the eastward direction immediately following the precipitation. Substorm auroral bulges are associated with spatially and temporally structured plasma convection (e.g., Gjerloev & Hoffman, 2001; Lyons & Nishimura, 2020), and the enhancement is possibly part of the substorm convection pattern.

Figure 10 shows the DMSP measurements before (by DMSP 17, left) and during the event (by DMSP 18, right). These are from the Southern Hemisphere. However, the time variation of the convection electric field in the closed field line region should apply to the Northen Hemisphere as the field is mapped along magnetic field lines from the magnetosphere. We primarily focus on the cross-track plasma velocity in Figures 10a and 10e, which is associated with the electric field in the along-track direction through the electric field drift. Since the spacecraft was located in the dusk sector, a positive value corresponds to a westward velocity, and hence a poleward-directed electric field. The most striking feature is the enhancement of the cross-track velocity (blue curve) in the sunward

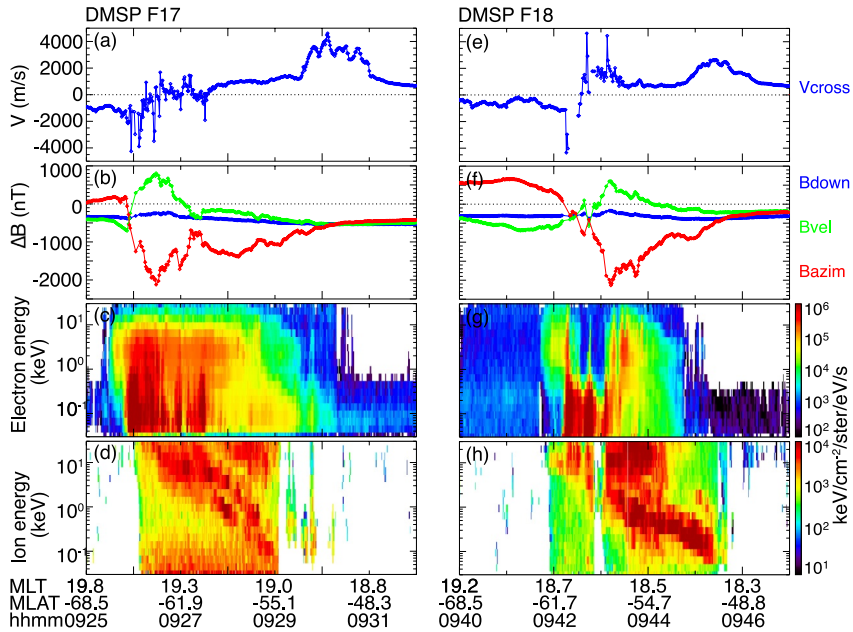

Figure 10. (a) Cross-track (blue) and vertical (red) ion velocity measured by DMSP F17 on 11 May 2024. (b) Magnetic perturbation. (c)–(d) Energy spectra of precipitating electrons and ions. (e)–(h) Similar to (a)–(d) but measured by DMSP F18.

or westward direction between around −56° to −60° MLAT. Specifically, the velocity oscillated around zero before the event, but turned strongly sunward or westward with most of the measurements >1,000 m/s, and two measurements exceeding 4,000 m/s during the event. The velocity/electric field enhancement occurred in the poleward portion of the auroral oval (oval identified based on precipitation of electrons and ions in Figures 10g and 10h), The enhancement was also embedded within R1 FACs (R1 currents identified based on negative gradient of the azimuthal component of the magnetic field in Figure 10f). This is consistent with PFISR measurements in Figure 9 as PFISR was positioned within the poleward portion of the Northern Hemisphere auroral electrojet. Note that PFISR was located in the pre-midnight sector at around 2230 MLT, and observed enhanced eastward convection as part of the dawn convection cell. DMSP traversed the dusk sector at around 1900 MLT, and observed enhanced westward convection as part of dusk convection cell. This indicates that the convection was enhanced over wide range of MLTs, possibly globally.

Although outside the scope of the current study, we note that the DMSP measurements contained additional interesting features, such as subauroral polarization stream signature, energy-dispersed ion precipitation, and localized depletion of electron precipitation. These features contain important information about the state of the magnetosphere and warrant detailed analysis.

4. Discussion: Solar Wind Driving Condition

Possible solar wind sources of the two events are discussed in this section. Figures 11a–11c show the OMNI solar wind and IMF conditions, which were taken from sensors onboard the L1-orbiting WIND mission and propagated to the Earth's bow shock nose. In Figure 11a, the IMF was northward during 0737–0757 UT, and turned southward, where the IMF Bz oscillated around −10 nT. It turned strongly southward to IMF Bz being about −35 nT at around 0828 UT, and remained steady until 0930 UT. After 0930 UT the IMF Bz started to fluctuate again and recovered to about −20 nT. The IMF By was positive most of the time except for a brief excursion to negative during 0759–0809 UT. Coinciding with the strong and steady southward IMF was a parcel of lower-density solar wind of ∼10 cm^{-3}, density being less than half of the surrounding, as shown in Figure 11b. The low density started at around 0833 UT, and showed multi-step jumps, first at around 0926 UT, then at around 0937 UT. Because the speed of the solar wind did not change much as shown in Figure 11c, the solar wind dynamic pressure was lower during the interval of lower solar wind density.

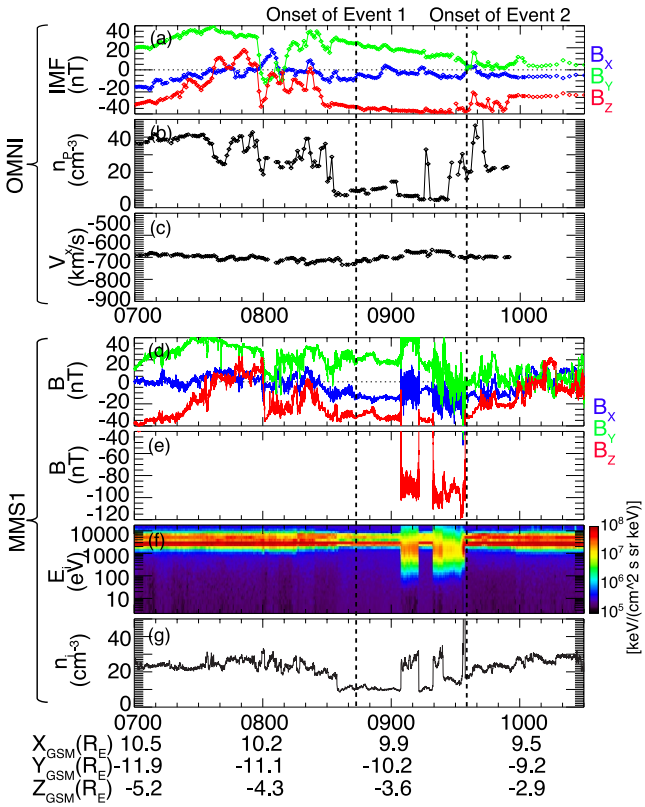

Figure 11. (a–c) OMNI IMF, solar wind number density, and solar wind velocity component in the Sun-Earth direction on 11 May 2024. (d–g) MMS1-measured magnetic field, ion energy spectrum, and ion number density. MMS1 was mainly located in the solar wind, but excursed to the magnetosheath briefly due to a change of the bow shock location. The MMS1 magnetic field was hence shown in two panels where the *Y* axis range of Panel d is suitable for displaying IMF, and the *Y* axis range of Panel e is suitable for displaying magnetic field in the magnetosheath.

The OMNI data were overall consistent with MMS measurements obtained just upstream of the bow shock, although depending on the structures of interest, the two data sets are shifted from each other by about 2–3 min. MMS additionally observed a sudden increase of magnetic field (Figure 11e) and ion density (Figure 11g) during 0905–0913 UT and 0919–0935 UT. The increase was because the bow shock expanded/protruded outward, engulfing the satellite. The outward expansion of the bow shock was also captured by THEMIS and CLUSTER located on the dayside (not shown). The expansion coincided with a decreased solar wind number density in OMNI data, which is associated with a decreased solar wind Mach number and hence decompression of the magnetosphere.

The solar wind driver of the second event is comparatively easy to identify, and is discussed first. The enhanced magnetospheric convection in the second event is well explained by being driven by a solar wind dynamic pressure increase. This is partly because the event onset (0935 UT) occurred nearly simultaneously with the magnetosphere compression by the enhanced dynamic pressure. The compression was captured by MMS and GOES, which observed contraction of the dayside magnetosphere and stretching of the magnetotail, respectively. Specifically, MMS returned to the solar wind at about 30 s before 0935 UT, indicating an inward motion of the bow shock (Figure 11). GOES 18 was located around the midnight and observed an increase of the magnetic inclination angle and an increase of the total magnetic field strength at around 0935 UT (Figure 6), which was a result of stretching of magnetic field lines. GOES 16 observed similar processes at dawn. The magnetic field strength more than doubled (from about 160 to 350 nT) and stayed elevated. The change started at around 0935 UT, the same time as GOES 18, suggesting that the magnetosphere was compressed on a global scale.

The enhanced convection and precipitation during the second event are also consistent with what is expected to occur following a solar wind pressure increase such as brightened auroras (Brittnacher et al., 2000; Holmes et al., 2014; Meurant et al., 2003, 2004; Zhou & Tsurutani, 1999; Zhou et al., 2009) and enhanced convection (Lukianova, 2003; Liou et al., 2004, 2017; Boudouridis et al., 2005). The brightened auroras are often diffuse, although discrete aurora brightening such as poleward boundary intensifications and auroral streamers have also been reported (Lyons et al., 2000). A mechanism of diffuse aurora brightening is adiabatic energization of particles associated with the increase of the magnetic field intensity in the magnetosphere. The energization results an increase of the perpendicular kinetic energy of particles, and hence an increase of the particle temperature anisotropy. This triggers loss cone instability and enhances growth of plasma waves which scatter particles into the loss cone by wave-particle interactions (Tsurutani et al., 2001; Zhou & Tsurutani, 1999). The particle energization also means an increase of energy flux into the ionosphere. An alternative mechanism is enlargement of the particle loss cone due to reductions in the mirror ratio (Liou et al., 2007). The enhanced convection can be attributed to the enhanced interplanetary electric field that often follows the solar wind pressure increase (Troshichev, 2022) and the increased coupling efficiency between the solar wind and the magnetosphere (Boudouridis et al., 2005).

An increase of the solar wind dynamic pressure has been noted to drive a dual-pulse response at high latitudes at ground, which is composed of a preliminary impulse (PI) followed by a main impulse (MI) (Araki, 1994; Stauning & Troshichev, 2008). The PI corresponds to two-cell ionospheric equivalent current system that has an opposite sense to DP2 currents, whereas the MI corresponds to a system of the same sense as DP2. The PI and MI current cells are usually generated at dayside cusp latitudes at either side of noon, and propagate anti-sunward (Nishimura et al., 2016; Madelaire et al., 2022). In our event, the bipolar impulse signatures are not pronounced in the SuperMAG data in Figure 7, probably because those transient disturbances are often tens or low hundreds of nT in magnitude, much smaller than the electrojet associated with the enhanced general convection. Madelaire et al. (2022) noted that under southward IMF, there is a general lack of PI and the MI is often poorly

resolved due to the significant enhancement of pre-existing currents. On the other hand, AMPERE data in Figure 8 shows a delayed enhancement of in situ magnetic field at 2300 and 1900 MLT relative to 1300 and 0700 MLT, which could be consistent with propagation of impulse-related signatures. Whether the delay is significant warrants further study because it could be due to satellites at 2300 and 1900 MLT positioned outside the latitude range of interest.

Both SuperMAG and AMPERE data show a larger magnetic field perturbation at dawn than dusk, and a similar asymmetry was reported by Zou et al. (2024). The asymmetry is possibly due to larger ionospheric conductivity at dawn because the diffuse electron precipitation is most intense at the post-midnight and morning hours.

However, open questions remain. Here we highlight two questions that may benefit from analysis of a larger event sample than the single case presented.

1. At what time scale does convection electric field respond to solar wind pressure increase? In the current event, the convection field at around 2230 MLT increased nearly instantaneously upon the arrival of the pressure increase. However, ample evidence shows that following IMF changes, the convection field reconfigures with a delay (Etemadi et al., 1988; Fiori et al., 2012; Huang et al., 2000; Lockwood et al., 1986; Murr & Hughes, 2001; Nishitani et al., 2002; Saunders et al., 1992; Todd et al., 1988). The delay time depends on the location of measurements, being shortest (zero to a few minutes) on the dayside, and longest (10 to 30 minutes) around midnight. Whether the instantaneous electric field increase is representative of all solar wind pressure increase, and why it is not delayed similar to what follows an IMF change warrant further investigation.
2. What determines the relative importance of convection electric field and particle precipitation in driving extreme auroral electrojets? Although the convection electric field was shown to make the major contribution in the current study, the opposite was suggested by Zou et al. (2024) who proposed that particle precipitation was more important. One hypothesis is that the precondition of the magnetosphere matters. The current event was preceded by a super intense substorm, which means that the near-Earth plasma sheet was filled with energetic particles and that the cross-tail current was already disrupted. The event discussed by Zou et al. (2024) was not preceded by substorms, and the electrojet was enhanced over a latitudinally narrow band.

Whether the first event was externally driven, and what served as the driver, are elusive. The first event, which was a substorm, commenced sometime between 0840 and 0844 UT. The uncertainty of the onset time stems from the fact that the auroral electrojet takes time to build. The onset occurred <20 min after the IMF turned strongly southward and <10 min after the solar wind density and pressure halved. We speculate that the pressure decrease did not contribute to the substorm triggering for two reasons. Firstly, the pressure decrease seems to have limited geoeffect based on existing observations. For instance, MMS (or THEMIS/Cluster) did not capture expansion of the bow shock on the dayside, and GOES did not detect thickening of the nightside plasma sheet. Secondly, although there are studies that show negative pressure pulses can trigger substorms (McPherron et al., 2023), pressure increases are shown to be more routinely capable of triggering substorms (Iyemori & Tsunomura, 1983; Kawasaki et al., 1971; Keika et al., 2009; Kokubun et al., 1977; Lyons et al., 2005; Zhou & Tsurutani, 2001) (Note that pressure increases do not always trigger substorms, and concurrent IMF conditions also affect substorm occurrence (e.g., Lyons et al., 2005)). It has been proposed that the compression associated with the high-pressure solar wind causes the lobe magnetic field to increase and the plasma sheet to thin. As the thinning reaches an unstable state, magnetic reconnection or plasma current instabilities initiate and a substorm occurs (Hubert et al., 2006). The sudden decrease of solar wind pressure should have the opposite effects to a pressure increase, and hence may potentially inhibit a substorm from developing.

The turning of the IMF to strongly southward could play an important role in the substorm development by allowing large amounts of energy to enter the magnetosphere. For typical substorms, the substorm intensity is directly governed by the amount of energy accumulated in the magnetotail prior to the onset, and this amount is closely related to the strength of the southward IMF (Milan et al., 2009). For high-intensity disturbances like supersubstorms, energy accumulated during the growth phase is often insufficient, and continuous energy input during substorm expansion and recovery phases is needed (Tsurutani & Hajra, 2023). In fact, the input during the expansion and recovery phases often exceeds that during the growth phase, being the main energy supply for the disturbance (Tsurutani & Hajra, 2023). The IMF remained strongly southward (being close to −40 nT) throughout all phases of the supersubstorm, making rapid and continuous energy input possible.

A widely discussed solar wind trigger of substorms is northward turnings of the IMF (Hsu & McPherron, 2002, 2003; Lyons et al., 1997). Although a northward turning did occur, this was about an hour earlier than the substorm onset, unlikely acting as a trigger of the disturbance. No other substorms were detected around the time of the IMF change.

Similarly to the second event, the first event also has unanswered questions as follows.

1. What controls the length of the supersubstorm? The supersubstorm was brief, lasting only about 40 min. This is shorter than most of substorms, where the SML index decreases and recovers over the duration of about 2 hours (see Forsyth et al., 2015). The IMF was dominated by the Bz component, and this component stayed strongly southward toward and even after the end of the supersubstorm. Although the IMF B_Y decreased, the decrease was gradual. What other processes might have caused the supersubstorm activity to end earlier than normal remains unknown.
2. What gives rise to the high intensity of this substorm, making it a supersubstorm? Although the event was associated with strongly southward IMF, a similar IMF occurred 2 hours ago lasting for about 1.5 hr. Despite the large amount of energy accumulated in the magnetotail during that time, no substorms or other auroral electrojet disturbance occurred. One hypothesis is that conditions internal to the magnetosphere might have stabilized the magnetosphere to substorm instability. One candidate is a strong ring current, because the ring current is associated with a northward magnetic component in the near-Earth tail that can inhibit the onset of magnetic reconnection until the build-up of open magnetic flux in the lobes produces a stretched topology (Milan et al., 2009). However, the exact condition that leads to/prevents supersubstorm development warrants further exploration.

5. Summary

Two extreme auroral electrojet intervals occurred in the nightside auroral zone during the May 2024 geomagnetic storm. Although both satisfy the definition of supersubstorms, the two events exhibit distinctly different features, suggesting that they were driven by different types of disturbances. Their main differences are summarized as follows.

1. The auroral electrojet in the first event was intensified over a narrow latitude band (of about 2°) and a localized MLT (in the pre-midnight and midnight sector) which then expanded poleward and azimuthally. The electrojet in the second event intensified across a broad latitude range (about 10°) and across all MLTs instantaneously.
2. The magnetic perturbations associated with FACs in the first event strengthened drastically by >1,000 nT in a narrow latitude band and in the pre-midnight sector which then propagated toward dawn. The magnetic perturbations in the second event showed a modest enhancement across polar latitudes and all MLTs nearly simultaneously. The enhancement was of several hundred nT and largest at dawn and dusk.
3. The localized activation of the auroral electrojet and FACs during the first event followed by a poleward and azimuthal expansion is characteristic of a substorm expansion phase. Indeed, auroral observations showed poleward expansion of auroras. Measurements made at geosynchronous orbit showed thickening of the plasma sheet, magnetic field dipolarization, and energetic particle injections, all classic signatures of a substorm.
4. The instantaneous enhancement of the auroral electrojet and FACs over the entire polar region suggests that the second event was not a substorm, but enhancement of general magnetospheric convection. Measurements obtained from radar and LEO satellites showed a sharp increase of the convection electric field. On the other hand, the auroras did not expand but brightened simultaneously across the entire sky. The magnetic field in the magnetotail did not dIpolarize but became further stretched.
5. The first event was not associated with a clear solar wind driver, whereas the second event was driven by a solar wind dynamic pressure increase. The first event was preceded by an increase of the southward IMF component to about −40 nT, and this IMF turning may have played an important role in the substorm development by allowing rapid and continuous energy input into the magnetosphere in all phases of the substorm. The first event was also preceded by a solar wind pressure decrease, but the importance of this is unclear.

Therefore, only the first supersubstorm is a substorm. This result is important because it demonstrates that extreme electrojet activity has more than one type of driver. Care should be exercised when using the term supersubstorm because the name encompasses phenomena other than substorms. The result also highlights the

equally important roles of internal instability in the magnetotail and external driving of the solar wind in space weather, as both processes are effective in driving explosive and extreme disturbances at nightside high latitudes.

Conflict of Interest

The authors declare no conflicts of interest relevant to this study.

Data Availability Statement

SuperMAG data are available from https://supermag.jhuapl.edu/info/. AMPERE-NEXT data are available from https://ampere.jhuapl.edu/. TREx data are available from https://data.phys.ucalgary.ca/sort_by_project/TREx/. GOES data are available from https://data.ngdc.noaa.gov/platforms/solar-space-observing-satellites/goes/goes16/l2/data/. PFISR data are available from https://amisr.com/amisr/. DMSP data are available from https://www.ncei.noaa.gov/data/dmsp-space-weather-sensors/access/. MMS data are available from https://lasp.colorado.edu/mms/sdc/public/.

Acknowledgments
YZ is supported by NASA 80NSSC23K1409 and 80NSSC21K0729. SO is supported by NASA 80NSSC21K0036 and NSF AGS-2224986. JG is supported by NASA 80NSSC21K0036, NSF AGS-1852715, and NSF PD-98-5750. The work at JHU/APL is also supported by the NASA DRIVE Science Center for Geospace Storms (CGS) under award 80NSSC22M0163. C.-P. Wang is supported by NASA 80NSSC22K1012 and NSF-GEM 2224108. We gratefully acknowledge the SuperMAG collaborators (https://supermag.jhuapl.edu/info/?page=acknowledgement). We thank the AMPERE team and the AMPERE Science Data Center for providing data products derived from the Iridium Communications constellation, enabled by support from the National Science Foundation. We also thank the TREx team led by Eric Donovan, and TREx is jointly funded by CFI, Alberta Economic Development and Trade, and the University of Calgary.

References

Ahn, B. H., Akasofu, S. I., & Kamide, Y. (1983). The Joule heat production rate and the particle energy injection rate as a function of the geomagnetic indices AE and AL. *Journal of Geophysical Research*, *88*(A8), 6275–6287. https://doi.org/10.1029/ja088ia08p06275

Akasofu, S. I. (1964). The development of the auroral substorm. *Planetary and Space Science*, *12*(4), 273–282. https://doi.org/10.1016/0032-0633(64)90151-5

Akasofu, S. I. (1981). Energy coupling between the solar wind and the magnetosphere. *Space Science Reviews*, *28*(2), 121–190. https://doi.org/10.1007/bf00218810

Akasofu, S. I., Chapman, S., & Meng, C. I. (1965). The polar electrojet. *Journal of Atmospheric and Terrestrial Physics*, *27*(11–12), 1275–1305. https://doi.org/10.1016/0021-9169(65)90087-5

Anderson, B. J., Angappan, R., Barik, A., Vines, S. K., Stanley, S., Bernasconi, P. N., et al. (2020). Iridium communications satellite constellation data for study of Earth's magnetic field. *Geochemistry, Geophysics, Geosystems*, *22*(22), e2020GC009515. https://doi.org/10.1029/2020gc009515

Araki, T. (1994). A physical model of geomagnetic sudden commencement. In M. J. Engebretson, K. Takahashi, & M. Scholer (Eds.), *Solar wind sources of magnetospheric ultra-low-frequency waves* (Vol. 81, pp. 183–200). https://doi.org/10.1029/GM081p0183

Boudouridis, A., Zesta, E., Lyons, L. R., Anderson, P. C., & Lummerzheim, D. (2005). Enhanced solar wind geoeffectiveness after a sudden increase in dynamic pressure during southward IMF orientation. *Journal of Geophysical Research*, *110*(A5), A05214. https://doi.org/10.1029/2004ja010704

Brittnacher, M., Wilber, M., Fillingim, M., Chua, D., Parks, G., Spann, J., & Germany, G. (2000). Global auroral response to a solar wind pressure pulse. *Advances in Space Research*, *25*(7), 1377–1385. https://doi.org/10.1016/s0273-1177(99)00647-x

Clauer, C. R., & Kamide, Y. (1985). DP 1 and DP 2 current systems for the March 22, 1979 substorms. *Journal of Geophysical Research*, *90*(A2), 1343–1354. https://doi.org/10.1029/JA090iA02p01343

Despirak, I. V., Kleimenova, N. G., Gromova, L. I., Gromov, S. V., & Malysheva, L. M. (2020). Supersubstorms during storms of september 7–8, 2017. *Geomagnetism and Aeronomy*, *60*(3), 292–300. https://doi.org/10.1134/S0016793220030044

Despirak, I. V., Kleimenova, N. G., Lyubchich, A. A., Setsko, P. V., Gromova, L. I., & Werner, R. (2022). Global development of the supersubstorm of May 28, 2011. *Geomagnetism and Aeronomy*, *62*(3), 199–208. https://doi.org/10.1134/s0016793222030069

Etemadi, A., Cowley, S. W. H., Lockwood, M., Bromage, B. J. I., Willis, D. M., & Lühr, H. (1988). The dependence of high-latitude dayside ionospheric flows on the north-south component of the IMF: A high time resolution correlation analysis using EISCAT "POLAR" and AMPTE UKS and IRM data. *Planetary and Space Science*, *36*(5), 471–498. https://doi.org/10.1016/0032-0633(88)90107-9

Fiori, R. A. D., Boteler, D. H., & Koustov, A. V. (2012). Response of ionospheric convection to sharp southward IMF turnings inferred from magnetometer and radar data. *Journal of Geophysical Research*, *117*(A9), A09302. https://doi.org/10.1029/2012JA017755

Forsyth, C., Rae, I. J., Coxon, J. C., Freeman, M. P., Jackman, C. M., Gjerloev, J., & Fazakerley, A. N. (2015). A new technique for determining substorm onsets and phases from indices of the electrojet (SOPHIE). *Journal of Geophysical Research: Space Physics*, *120*(12), 10592–10606. https://doi.org/10.1002/2015JA021343

Fukushima, N. (1971). Electric current systems for polar substorms and their magnetic effect below and above the ionosphere. *Radio Science*, *6*(2), 269–275. https://doi.org/10.1029/rs006i002p00269

Gjerloev, J. W. (2012). The SuperMAG data processing technique. *Journal of Geophysical Research*, *117*(A9), A09213. https://doi.org/10.1029/2012JA017683

Gjerloev, J. W., & Hoffman, R. A. (2001). The convection electric field in auroral substorms. *Journal of Geophysical Research*, *106*(A7), 12919–12931. https://doi.org/10.1029/1999JA000240

Hajra, R., Echer, E., & Bolzan, M. J. A. (2023). Earth's magnetotail variability during supersubstorms (SSSs): A study on solar wind–magnetosphere–ionosphere coupling. *Advances in Space Research*, *72*(4), 1208–1223. https://doi.org/10.1016/j.asr.2023.04.013

Hajra, R., & Tsurutani, B. T. (2018). Interplanetary shocks inducing magnetospheric supersubstorms (SML < −2500 nT): Unusual auroral morphologies and energy flow. *The Astrophysical Journal*, *858*(2), 123. https://doi.org/10.3847/1538-4357/aabaed

Hajra, R., Tsurutani, B. T., Echer, E., Gonzalez, W. D., & Gjerloev, J. W. (2016). Supersubstorms (SML < −2500 nT): Magnetic storm and solar cycle dependences. *Journal of Geophysical Research: Space Physics*, *121*(8), 7805–7816. https://doi.org/10.1002/2015JA021835

Holmes, J. M., Johnsen, M. G., Deehr, C. S., Zhou, X.-Y., & Lorentzen, D. A. (2014). Circumpolar ground-based optical measurements of proton and electron shock aurora. *Journal of Geophysical Research: Space Physics*, *119*(5), 3895–3914. https://doi.org/10.1002/2013ja019574

Hsu, T.-S., & McPherron, R. L. (2002). An evaluation of the statistical significance of the association between northward turnings of the interplanetary magnetic field and substorm expansion onsets. *Journal of Geophysical Research*, *107*(A11), 1398. https://doi.org/10.1029/2000JA000125

Hsu, T.-S., & McPherron, R. L. (2003). Occurrence frequencies of IMF triggered and nontriggered substorms. *Journal of Geophysical Research*, *108*(A7), 1307. https://doi.org/10.1029/2002JA009442

Huang, C.-S., Murr, D., Sofko, G. J., Hughes, W. J., & Moretto, T. (2000). Ionospheric convection response to changes of interplanetary magnetic field B_z component during strong b_y component. *Journal of Geophysical Research*, *105*(A3), 5231–5243. https://doi.org/10.1029/1999JA000099

Hubert, B., Palmroth, M., Laitinen, T. V., Janhunen, P., Milan, S. E., Grocott, A., et al. (2006). Compression of the Earth's magnetotail by interplanetary shocks directly drives transient magnetic flux closure. *Geophysical Research Letters*, *33*(10), L10105. https://doi.org/10.1029/2006GL026008

Iyemori, T., & Tsunomura, S. (1983). Characteristics of the association between an SC and a substorm onset. *Memoirs of National Institute of Polar Research*, *26*, 139–148.

Kamide, Y., & Kokubun, S. (1996). Two-component auroral electrojet: Importance for substorm studies. *Journal of Geophysical Research*, *101*(13), 027–13046. https://doi.org/10.1029/96ja00142

Kawasaki, K., Akasofu, S.-I., Yasuhara, F., & Meng, C.-I. (1971). Storm sudden commencements and polar magnetic substorms. *Journal of Geophysical Research (1896-1977)*, *76*(28), 6781–6789. https://doi.org/10.1029/JA076i028p06781

Keika, K., Nakamura, R., Baumjohann, W., Angelopoulos, V., Chi, P. J., Glassmeier, K. H., et al. (2009). Substorm expansion triggered by a sudden impulse front propagating from the dayside magnetopause. *Journal of Geophysical Research*, *114*(A1), A00C24. https://doi.org/10.1029/2008ja013445

Kokubun, S., McPherron, R. L., & Russell, C. T. (1977). Triggering of substorms by solar wind discontinuities. *Journal of Geophysical Research (1896-1977)*, *82*(1), 74–86. https://doi.org/10.1029/JA082i001p00074

Liou, K., Newell, P. T., Meng, C.-I., Wu, C.-C., & Lepping, R. P. (2004). On the relationship between shock-induced polar magnetic bays and solar wind parameters. *Journal of Geophysical Research*, *109*(A6), A06306. https://doi.org/10.1029/2004ja010400

Liou, K., Newell, P. T., Shue, J.-H., Meng, C.-I., Miyashita, Y., Kojima, H., & Matsumoto, H. (2007). "Compression aurora": Particle precipitation driven by long-duration high solar wind ram pressure. *Journal of Geophysical Research*, *112*(A11), A11216. https://doi.org/10.1029/2007ja012443

Liou, K., Sotirelis, T., & Gjerloev, J. (2017). Statistical study of polar negative magnetic bays driven by interplanetary fast-mode shocks. *Journal of Geophysical Research: Space Physics*, *122*(7), 7463–7472. https://doi.org/10.1002/2017ja024465

Lockwood, M., van Eyken, A. P., Bromage, B. J. I., Willis, D. M., & Cowley, S. W. H. (1986). Eastward propagation of a plasma convection enhancement following a southward turning of the interplanetary magnetic field. *Geophysical Research Letters*, *13*(1), 72–75. https://doi.org/10.1029/GL013i001p00072

Lukianova, R. (2003). Magnetospheric response to sudden changes in solar wind dynamic pressure inferred from polar cap index. *Journal of Geophysical Research*, *108*(A12), 1428. https://doi.org/10.1029/2002ja009790

Lyons, L. R., Blanchard, G. T., Samson, J. C., Lepping, R. P., Yamamoto, T., & Moretto, T. (1997). Coordinated observations demonstrating external substorm triggering. *Journal of Geophysical Research*, *102*(A12), 27039–27051. https://doi.org/10.1029/97ja02639

Lyons, L. R., Lee, D.-Y., Wang, C.-P., & Mende, S. B. (2005). Global auroral responses to abrupt solar wind changes: Dynamic pressure, substorm, and null events. *Journal of Geophysical Research*, *110*(A8), A08208. https://doi.org/10.1029/2005JA011089

Lyons, L. R., & Nishimura, Y. (2020). Substorm onset and development: The crucial role of flow channels. *Journal of Atmospheric and Solar-Terrestrial Physics*, *211*, 105474. https://doi.org/10.1016/j.jastp.2020.105474

Lyons, L. R., Zesta, E., Samson, J. C., & Reeves, G. D. (2000). Auroral disturbances during the January 10, 1997 magnetic storm. *Geophysical Research Letters*, *27*(20), 3237–3240. https://doi.org/10.1029/1999gl000014

Madelaire, M., Laundal, K. M., Reistad, J. P., Hatch, S. M., & Ohma, A. (2022). Transient high latitude geomagnetic response to rapid increases in solar wind dynamic pressure. *Frontiers in Astronomy and Space Sciences*, *9*, 953954. https://doi.org/10.3389/fspas.2022.953954

McPherron, R. L. (2023). Substorm triggering by the solar wind. *Journal of Geophysical Research: Space Physics*, *128*(6), e2022JA031147. https://doi.org/10.1029/2022JA031147

Meurant, M., Gérard, J.-C., Blockx, C., Hubert, B., & Coumans, V. (2004). Propagation of electron and proton shock-induced aurora and the role of the interplanetary magnetic field and solar wind. *Journal of Geophysical Research*, *109*(A10), A10210. https://doi.org/10.1029/2004ja010453

Meurant, M., Gérard, J.-C., Hubert, B., Coumans, V., Blockx, C., Østgaard, N., & Mende, S. B. (2003). Dynamics of global scale electron and proton precipitation induced by a solar wind pressure pulse. *Geophysical Research Letters*, *30*(20), 2032. https://doi.org/10.1029/2003gl018017

Milan, S., Grocott, A., Forsyth, C., Imber, S., Boakes, P., & Hubert, B. (2009). A superposed epoch analysis of auroral evolution during substorm growth, onset and recovery: Open magnetic flux control of substorm intensity. *Annales Geophysicae*, *27*(2), 659–668. https://doi.org/10.5194/angeo-27-659-2009

Murr, D. L., & Hughes, W. J. (2001). Reconfiguration timescales of ionospheric convection. *Geophysical Research Letters*, *28*(11), 2145–2148. https://doi.org/10.1029/2000GL012765

Nagai, T. (1991). An empirical model of substorm-related magnetic field variations at synchronous orbit. In J. R. Kan, T. A. Potemra, S. Kokubun, & T. Iijima (Eds.), *Magnetospheric substorms*. https://doi.org/10.1029/GM064p0091

Newell, P. T., & Gjerloev, J. W. (2011). Evaluation of SuperMAG auroral electrojet indices as indicators of substorms and auroral power. *Journal of Geophysical Research*, *116*(A12), A12211. https://doi.org/10.1029/2011JA016779

Newell, P. T., & Gjerloev, J. W. (2015). Local geomagnetic indices and the prediction of auroral power. *Journal of Geophysical Research: Space Physics*, *119*(12), 9790–9803. https://doi.org/10.1002/2014JA020524

Nisbet, J. S. (1982). Relations between the Birkeland currents, the auroral electrojet indices and high latitude Joule heating. *Journal of Atmospheric and Terrestrial Physics*, *44*(9), 797–809. https://doi.org/10.1016/0021-9169(82)90009-5

Nishida, A. (1968). Geomagnetic DP-2 fluctuations and associated mangetospheric phenomena. *Journal of Geophysical Research*, *13*, 1795.

Nishimura, Y., Kikuchi, T., Ebihara, Y., Yoshikawa, A., Imajo, S., Li, W., & Utada, H. (2016). Evolution of the current system during solar wind pressure pulses based on aurora and magnetometer observations. *Earth Planets and Space*, *68*, 1–16. https://doi.org/10.1186/s40623-016-0517-y

Nishitani, N., Ogawa, T., Sato, N., Yamagishi, H., Pinnock, M., Villain, J.-P., et al. (2002). A study of the dusk convection cell's response to an IMF southward turning. *Journal of Geophysical Research*, *107*(A3), 1036. https://doi.org/10.1029/2001JA900095

Obayashi, T. (1967). The interaction of the solar wind with the geomagnetic field during disturbed conditions. In J. W. King & W. S. Newman (Eds.), *Solar-terrestrial physics*. Academic Press.

Ohtani, S. (2022). New insights from the 2003 Halloween storm into the Colaba 1600 nT magnetic depression during the 1859 Carrington storm. *Journal of Geophysical Research: Space Physics*, *127*(9), e2022JA030596. https://doi.org/10.1029/2022JA030596

Picone, J. M., Hedin, A. E., Drob, D. P., & Aikin, A. C. (2002). NRLMSISE-00 empirical model of the atmosphere: Statistical comparisons and scientific issues. *Journal of Geophysical Research*, *107*(A12), SIA15-1–SIA15-16. https://doi.org/10.1029/2002ja009430

Saunders, M. A., Freeman, M. P., Southwood, D. J., Cowley, S. W. H., Lockwood, M., Samson, J. C., et al. (1992). Dayside ionospheric convection changes in response to long-period interplanetary magnetic field oscillations: Determination of the ionospheric phase velocity. *Journal of Geophysical Research*, *97*(A12), 19373–19380. https://doi.org/10.1029/92JA01383

Schunk, R., & Nagy, A. (2009). *Ionospheres: Physics, plasma physics, and chemistry*. Cambridge University Press.

Stauning, P., & Troshichev, O. A. (2008). Polar cap convection and PC index during sudden changes in solar wind dynamic pressure. *Journal of Geophysical Research*, *113*(A8), A08227. https://doi.org/10.1029/2007JA012783

Thébault, E., Finlay, C. C., Beggan, C. D., Alken, P., Aubert, J., Barrois, O., et al. (2015). International geomagnetic reference field: The 12th generation. *Earth Planets and Space*, *67*(1), 1–19. https://doi.org/10.1186/s40623-015-0228-9

Todd, H., Cowley, S. W. H., Lockwood, M., Willis, D. M., & Lühr, H. (1988). Response time of the high-latitude dayside ionosphere to sudden changes in the north-south component of the IMF. *Planetary and Space Science*, *36*(12), 1415–1428. https://doi.org/10.1016/0032-0633(88)90008-6

Troshichev, O. A. (2022). PC index as a ground-based indicator of the solar wind energy incoming into the magnetosphere: (1) relation of PC index to the solar wind electric field EKL. *Frontiers in Astronomy and Space Sciences*, *9*, 1069470. https://doi.org/10.3389/fspas.2022.1069470

Tsurutani, B. T., & Hajra, R. (2023). Energetics of shock-triggered supersubstorms (SML < −2500 nT). *The Astrophysical Journal*, *946*(1), 17. https://doi.org/10.3847/1538-4357/acb143

Tsurutani, B. T., Hajra, R., Echer, E., & Gjerloev, J. W. (2015). Extremely intense (SML<-2500 nT) substorms: Isolated events that are externally triggered? *Annales Geophysicae*, *33*(5), 519–524. https://doi.org/10.5194/angeo-33-519-2015

Tsurutani, B. T., Zhou, X. Y., Arballo, J. K., Gonzalez, W. D., Lakhina, G. S., Vasyliunas, V., et al. (2001). Auroral zone dayside precipitation during magnetic storm initial phases. *Journal of Atmospheric and Solar-Terrestrial Physics*, *63*(5), 513–522. https://doi.org/10.1016/s1364-6826(00)00161-9

Vorobev, A. V., Pilipenko, V. A., Sakharov, Y. A., & Selivanov, V. N. (2019). Statistical relationships between variations of the geomagnetic field, auroral electrojet, and geomagnetically induced currents. *Solar-Terrestrial Physics*, *5*(1), 35–42. https://doi.org/10.12737/stp-51201905

Wang, Z., & Zou, S. (2022). Compass: A new COnductance model based on PFISR and SWARM satellite observations. *Space Weather*, *20*(2), e2021SW002958. https://doi.org/10.1029/2021sw002958

Waters, C. L., Anderson, B. J., Green, D. L., Korth, H., Barnes, R. J., & Vanhamaki, H. (2020). Science data products for AMPERE. In M. W. Dunlop & H. Luhr (Eds.), *Ionospheric multi-spacecraft analysis tools, ISSI scientific report series* (Vol. 17, pp. 141–165). https://doi.org/10.1007/978-3-030-26732-2

Watson, C. J., & Jayachandran, P. T. (2009). Azimuthal expansion of the dipolarization at geosynchronous orbits associated with substorms. *Annals of Geophysics*, *27*(3), 1113–1118. https://doi.org/10.5194/angeo-27-1113-2009

Xu, W., & Sun, W. (2000). A study on the multi-component substrom current. *Advances In Polar Science*, *11*(1-English), 53–58.

Zhou, X., & Tsurutani, B. T. (1999). Rapid intensification and propagation of the dayside aurora: Large scale interplanetary pressure pulses (fast shocks). *Geophysical Research Letters*, *26*(8), 1097–1100. https://doi.org/10.1029/1999gl900173

Zhou, X., & Tsurutani, B. T. (2001). Interplanetary shock triggering of nightside geomagnetic activity: Substorms, pseudobreakups, and quiescent events. *Journal of Geophysical Research*, *106*(A9), 18957–18967. https://doi.org/10.1029/2000ja003028

Zhou, X.-Y., Fukui, K., Carlson, H. C., Moen, J. I., & Strangeway, R. J. (2009). Shock aurora: Ground-based imager observations. *Journal of Geophysical Research*, *114*(A12), A12216. https://doi.org/10.1029/2009ja014186

Zou, Y., Gjerloev, J. W., Ohtani, S., Friel, M., Liang, J., Lyons, L. L., et al. (2024). An extreme auroral electrojet spike during 2023 April 24th storm. *AGU Advances*, *5*(3), e2023AV001101. https://doi.org/10.1029/2023AV001101